ACS NANO

www.acsnano.org

ARTICLE

Lithiation Induced Phases in 1T′-$MoTe_2$ Nanoflakes

Shiyu Xu, Kenneth Evans-Lutterodt, Shunran Li, Natalie L. Williams, Bowen Hou, Jason J. Huang, Matthew G. Boebinger, Sihun Lee, Mengjing Wang, Andrej Singer, Peijun Guo, Diana Y. Qiu, and Judy J. Cha*

Cite This: *ACS Nano* 2024, 18, 17349–17358

Read Online

ACCESS | Metrics & More | Article Recommendations | Supporting Information

ABSTRACT: **Multiple polytypes of $MoTe_2$ with distinct structures and intriguing electronic properties can be accessed by various physical and chemical approaches. Here, we report electrochemical lithium (Li) intercalation into 1T′-$MoTe_2$ nanoflakes, leading to the discovery of two previously unreported lithiated phases. Distinguished by their structural differences from the pristine 1T′ phase, these distinct phases were characterized using *in situ* polarization Raman spectroscopy and *in situ* single-crystal X-ray diffraction. The lithiated phases exhibit increasing resistivity with decreasing temperature, and their carrier densities are two to 4 orders of magnitude smaller than the metallic 1T′ phase, as probed through *in situ* Hall measurements. The discovery of these gapped phases in initially metallic 1T′-$MoTe_2$ underscores electrochemical intercalation as a potent tool for tuning the phase stability and electron density in two-dimensional (2D) materials.**

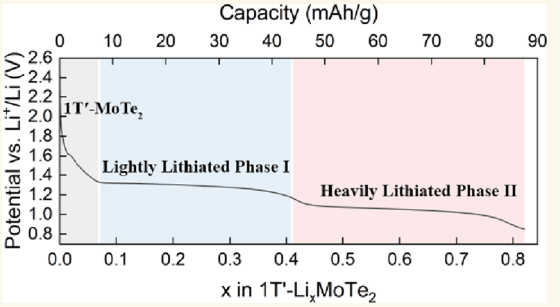

KEYWORDS: *lithium intercalation, phase transitions, molybdenum ditelluride, layered materials, in situ Raman characterization, electron doping*

INTRODUCTION

Two-dimensional (2D) transition metal dichalcogenides (TMDs) have garnered substantial attention in contemporary research. Their vast array of structural polymorphs underscores their significance in cutting-edge applications, including but not limited to optoelectronic and electronic devices, hydrogen evolution reaction (HER) catalysts, and biological sensors.[1−6] Among 2D TMDs, molybdenum ditelluride ($MoTe_2$) has three basic polytypes: a trigonal prismatic phase (α- or 2H-$MoTe_2$), a distorted octahedral phase (β- or 1T′-$MoTe_2$) and an orthorhombic phase (γ- or T_d-$MoTe_2$). These polytypes encompass a comprehensive range of electronic phases spanning from semiconductors,[7,8] to semimetals,[9] quantum spin Hall states,[10] type-II Weyl semimetals,[11] and superconducting states.[12−14] Phase transitions in $MoTe_2$ can be induced through various methods including defect engineering,[15] charge doping,[16,17] strain engineering,[18,19] intercalation,[20,21] thermal treatment,[9,22,23] and light irradiation.[24] These electronic phases, coupled with controllable phase transitions, position $MoTe_2$ as a promising candidate for a spectrum of applications, including memory devices,[25] transistors,[26] electrocatalysts,[27] and energy storage devices.[28]

The intercalation of lithium (Li) ions has emerged as a highly effective method for inducing structural transformations in 2D TMDs, giving rise to phases characterized by distinctive optical and electronic properties.[29,30] Numerous studies have focused on the phase transition from a semiconducting 2H phase to a metallic 1T (or 1T′) phase in MoS_2 and WS_2 induced by the intercalation of Li ions.[29,31,32] Few reports explored the effects of Li intercalation in other TMDs, such as Mo- and W- ditellurides. A new polytype of T_d-WTe_2, driven by lithiation, was recently discovered, exhibiting a unique crystal structure (T_d′)[33] with a bandgap opening of 0.14 eV.[34,35] For $MoTe_2$, lithiation studies are sparse. When 2H-$MoTe_2$ nanoflakes were immersed in *n*-butyllithium solution at 110 °C, the transition from the 2H phase to the 1T′ phase was observed only in the top and bottom layers of the nanoflakes.[21] A study conducted in 1987 revealed a reversible intercalation of Li into the van der Waals (vdW) gaps of 1T′-$MoTe_2$ bulk, resulting in the formation of two intermediate phases as the Li concentration increased, before the 1T′-$MoTe_2$ bulk decom-

Received: May 13, 2024
Revised: May 29, 2024
Accepted: June 5, 2024
Published: June 18, 2024

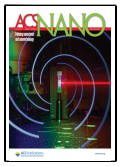

https://doi.org/10.1021/acsnano.4c06330
ACS Nano 2024, 18, 17349−17358

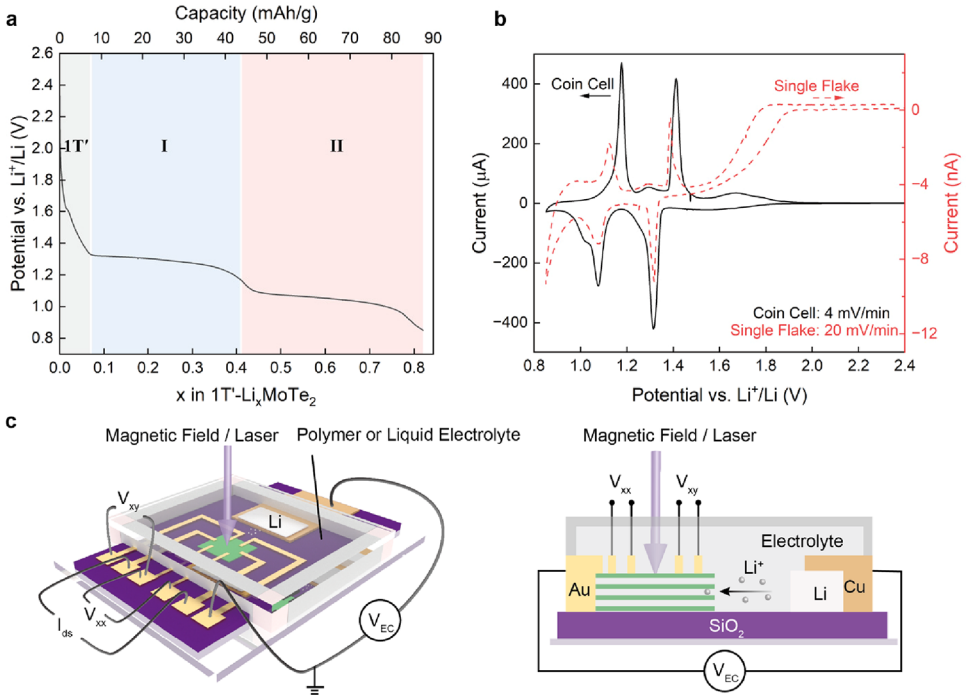

Figure 1. Electrochemical characteristics of 1T′-$MoTe_2$. (a) Galvanostatic discharging of 1T′-$MoTe_2$ powder in a coin cell at a current of 0.04 mA in the voltage window of 2.45 to 0.85 V vs Li^+/Li. (b) Cyclic voltammogram traces of 1T′-$MoTe_2$ vs Li^+/Li, in a coin cell at a scan rate of 4 mV/min (black curve) and in a single-flake intercalation cell at a scan rate of 20 mV/min (red dotted curve), respectively. The dimensions of this single nanoflake are 62 μm × 28 μm × ∼100 nm. (c) Schematics of a planar electrochemical intercalation cell with *in situ* Raman and *in situ* Hall measurement capabilities. V_{EC} stands for the electrochemical intercalation voltage applied between the single crystalline 1T′-$MoTe_2$ nanoflake and the Li^+/Li electrode. The Schematics were reprinted in part with permission under the terms of the CC-BY Creative Commons Attribution 4.0 International license (https://creativecommons.org/licenses/by/4.0) from Adv. Energy and Sustainability Research 2021, 2, 2100027. Copyright 2021, published by Wiley-VCH.

posed into a mixture of molybdenum (Mo), tellurium (Te) and lithium telluride (Li_2Te).[36] Yet, the structure and properties of these two intermediate phases remain unknown.

Here, we report electrochemical Li intercalation into 1T′-$MoTe_2$ nanoflakes. The 1T′ phase is stable down to 0.9 V of the applied electrochemical voltage vs Li^+/Li, using a polymer gel electrolyte and lithium metal as counter/reference electrode, and two phases that are distinct from the 1T′ phase are observed at 0.7 V vs Li^+/Li (lightly lithiated phase I) and 0.4 V vs Li^+/Li (heavily lithiated phase II). The lightly lithiated phase I is evidenced by the disappearance of the A_g peak at ∼78 cm^{-1} and the appearance of a peak at ∼85 cm^{-1} observed under Raman spectroscopy and an over 20-fold increase in electrical resistance. For the heavily lithiated phase II, we observe the emergence of new Raman peaks at 16.8 cm^{-1}, 109 and 133 cm^{-1}, a 5000-fold increase of electrical resistance, and *d*-spacing expansion of ∼7% for the (001) plane from single-crystal X-ray diffraction (XRD). Temperature-dependent four-point resistance measurements show a decrease in conductivity with a decreasing temperature, suggesting that phase II is a semiconducting phase. The 2D Hall carrier density falls from 10^{15} cm^{-2} in pristine 1T′-$MoTe_2$ to 10^{13} cm^{-2} in phase I and to 10^{11} cm^{-2} in phase II. Our results highlight the electrochemical intercalation of Li ions as a powerful tool to manipulate the phase stability and electron density of 2D TMDs.

RESULTS AND DISCUSSION

Electrochemical Characteristics of 1T′-$MoTe_2$ Powder. Coin-type electrochemical cells were assembled to investigate the lithiation process of 1T′-$MoTe_2$ powder (details in Experimental Methods). Two reduction−oxidation (redox) couples were observed at 1.3 and 1.1 V vs lithium electrode (Li^+/Li) in both the galvanostatic discharge curve (Figure 1a, voltage plateaus) and cyclic voltammetry trace (Figure 1b and Figure S1c, reduction peaks in the black curve). These repeatable redox features indicate reversible first-order phase transitions due to lithium intercalation of 1T′-$MoTe_2$, in agreement with the 1987 study.[36] The Li concentration shown in Figure 1a was calculated from the amount of charge transferred in the cell, indicating the lightly lithiated and heavily lithiated phases are nominally $Li_{0.5}MoTe_2$ and $LiMoTe_2$, although this estimation may not be quantitatively accurate due to side reactions of Li with the liquid electrolyte. Figure S1a and b show the irreversible decomposition reaction to Mo, Te, and Li_2Te below 0.6 V vs Li^+/Li.

Lithium Intercalation Induced Phase Transitions. While the coin-cell experiments identified two intermediate phases, physical properties of the lithiated phases cannot be measured using standard coin cells during intercalation, *in situ*. Instead, electrochemical intercalation cells that incorporate nanodevices facilitate *in situ* Raman spectroscopy,[37] *in situ* single-crystal X-ray diffraction (XRD)[33] and *in situ* Hall measurements[34] on isolated individual flakes as a function of intercalation, providing a comprehensive understanding of the phase transitions of 1T′-$MoTe_2$ flakes induced by lithium intercalation (Figure 1c, Experimental Methods). To avoid the mixed-phase effect of 1T′ and T_d phases in few-layered samples,[38,39] the mechanically exfoliated 1T′-$MoTe_2$ flakes were 40 to 110 nm thick. Both liquid and polymer-based

https://doi.org/10.1021/acsnano.4c06330
ACS Nano 2024, 18, 17349−17358

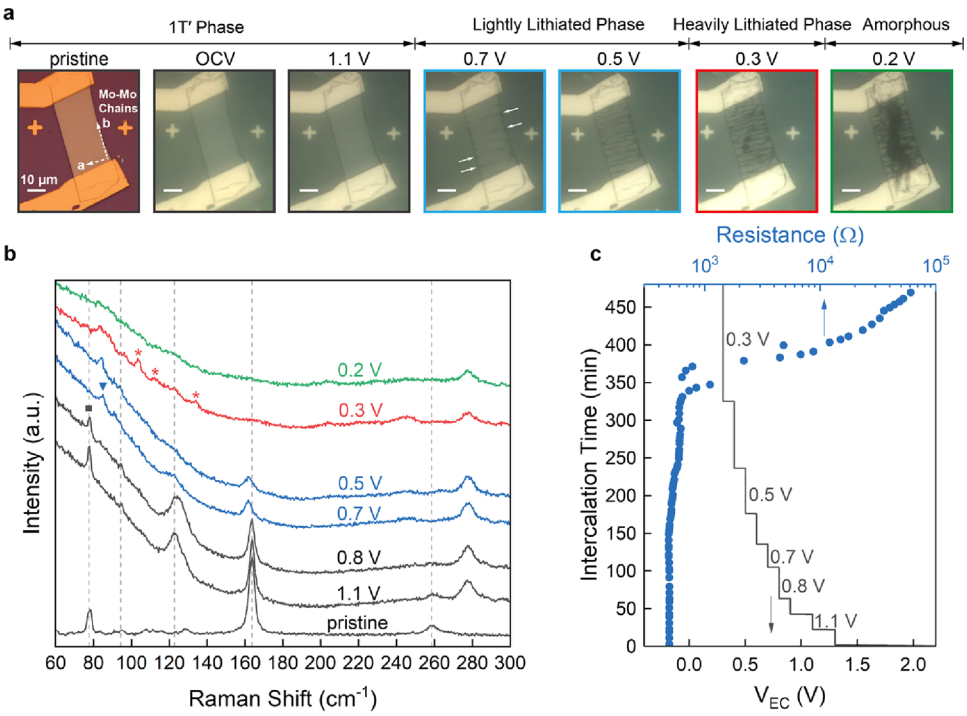

Figure 2. ***In situ*** **optical and Raman characterization and two-terminal resistance measurements of a 1T′-$MoTe_2$ nanoflake during lithiation (flake dimensions: 42 μm × 24 μm × ∼100 nm). (a) Optical images of a 1T′-$MoTe_2$ nanoflake as a function of V_{EC} using a polymer electrolyte; scale bar, 10 μm. The black, blue, red, and green frames represent the 1T′, lightly lithiated phase I, heavily lithiated phase II and amorphous state, respectively. (b)** ***In situ*** **Raman spectra of the 1T′-$MoTe_2$ nanoflake in (a) as a function of V_{EC}. The black, blue, red, and green spectra represent the 1T′, lightly lithiated phase I, heavily lithiated phase II and amorphous state, respectively. (c) Simultaneous two-terminal resistance (blue circles) and V_{EC} (black line) as a function of intercalation time. The V_{EC} is in line with the applied voltages in (a) and (b).**

electrolytes were used for lithium intercalation (details in Experimental Methods). The ionic conductivity of polymer-based electrolyte is ∼3 orders of magnitude smaller than that of liquid electrolyte at room temperature, which slows down the dynamics of the intercalation process, facilitating the characterization of phase transitions.[40,41] By applying a controlled electrochemical intercalation voltage (V_{EC}) between the single crystalline 1T′-$MoTe_2$ flake (cathode) and the lithium (Li, anode), lithium ions (Li^+) are inserted into the vdW gaps of the 1T′-$MoTe_2$ flake. The applied V_{EC} lies between the open-circuit voltage (OCV, typically 2.0−2.8 V vs Li^+/Li) and 0.1 V vs Li^+/Li. Changing the V_{EC} allows for the fine-tuning of intercalation concentrations, with a lower V_{EC} corresponding to a higher lithium concentration in the 1T′-$MoTe_2$ flake. The cyclic voltammetry trace of a single 1T′-$MoTe_2$ flake in an intercalation cell filled with liquid electrolyte (Figure 1b, the red dotted curve) matches that of 1T′-$MoTe_2$ powder in a coin-type cell, with two reduction peaks at 1.3 and 1.1 V vs Li^+/Li.

The lithiated intermediate phases are structurally distinct from the 1T′ phase of $MoTe_2$, characterized by unique Raman modes. We define the b (or y) axis to be the zigzag Mo−Mo chains, which is along the longer side of the exfoliated flake. Optical images in Figure 2a show discernible dark streaks along the crystallographic axis a, which is perpendicular to the Mo−Mo chain of pristine 1T′-$MoTe_2$, evident in both the lightly lithiated phase I (blue frames) and the heavily lithiated phase II (red frames). These streaks were identified as wrinkles in the flake due to the anisotropic in-plane strain introduced during phase transitions, as confirmed by scanning electron microscopy (SEM) on a postintercalation cell (Figure S2). Lightly lithiated phase I emerged at V_{EC} = 0.7 V vs Li^+/Li for a polymer cell (Figure 2b) and 1.3 V vs Li^+/Li for a liquid cell (Figure S3). At V_{EC} = 0.7 and 0.5 V vs Li^+/Li (phase I), the Raman peak corresponding to 1T′-$MoTe_2$ at ∼78 cm^{-1} vanished while the peak at ∼164 cm^{-1} broadened and shifted; concurrently, a new peak at ∼85 cm^{-1} emerged as shown in blue spectra in Figure 2b. The heavily lithiated phase II was observed at V_{EC} = 0.3 V vs Li^+/Li for a polymer cell (Figure 2b) and V_{EC} = 0.9 V vs Li^+/Li for a liquid cell (Figure S3, Supporting Information). At V_{EC} = 0.3 V vs Li^+/Li, several new Raman peaks emerged at ∼104 cm^{-1}, ∼ 113 cm^{-1} and ∼134 cm^{-1}, which are not associated with any known phases of $MoTe_2$, and the 1T′-$MoTe_2$ peak at ∼164 cm^{-1} completely disappeared (red spectrum in Figure 2b), which suggests that the heavily lithiated phase II is distinct from the 1T′ phase (Table S1 and S2). *In situ* Raman mapping captured a nonuniform intensity distribution of the peak associated with the heavily lithiated phase II where the dark streak regions show higher intensity than the rest of the flake (Figure S4). Lastly, the amorphization of $MoTe_2$ occurred when the $V_{EC} \leq$ 0.2 V vs Li^+/Li in a polymer cell and $V_{EC} \leq$ 0.6 V vs Li^+/Li in a liquid cell, as supported by the green featureless Raman spectrum in both Figure 2b and S3. The Raman peak at ∼277 cm^{-1} is attributed to the polymer electrolyte. The V_{EC} at which the two phases and amorphous state emerge are consistent: for polymer electrolyte, V_{EC} = 0.7 V, 0.3 V and ≤0.2 V vs Li^+/Li while for liquid electrolyte, V_{EC} = 1.3 V, 0.9 V and ≤0.6 V vs Li^+/Li.

https://doi.org/10.1021/acsnano.4c06330
ACS Nano 2024, 18, 17349−17358

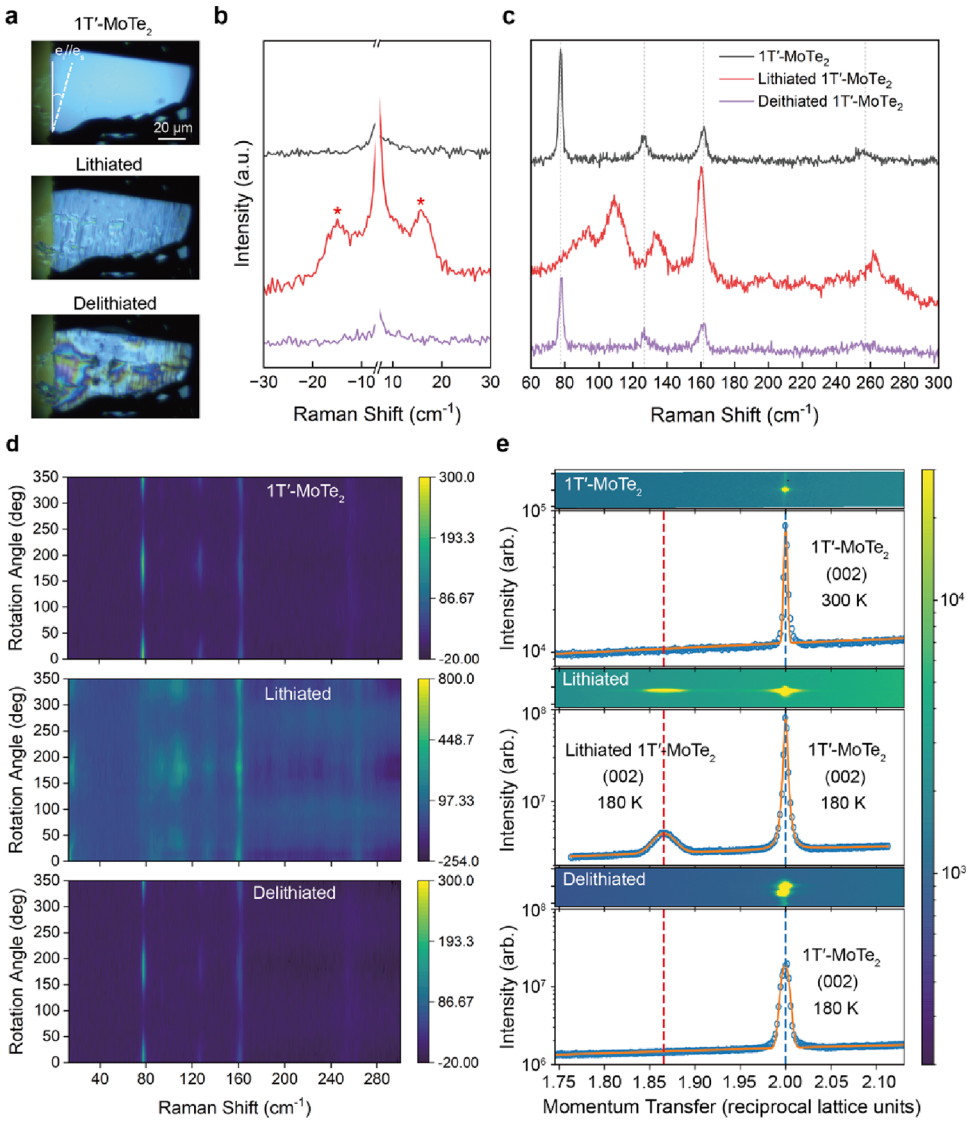

Figure 3. ***In situ*** **angle-resolved Raman and X-ray diffraction characterization of 1T′-$MoTe_2$ nanoflakes during phase transition. (a) Optical images of the pristine 1T′-$MoTe_2$ (top), lithiated 1T′-$MoTe_2$ (middle) and delithiated 1T′-$MoTe_2$ (bottom), corresponding to the Raman spectra in (b) and (c); scale bar, 20 μm (flake dimensions: 92 μm × 47 μm × ∼100 nm). (b, c) Low-frequency (b) and high-frequency (c) Raman spectra of the pristine 1T′-$MoTe_2$ (black, top), lithiated 1T′-$MoTe_2$ (red, middle) and delithiated 1T′-$MoTe_2$ (purple, bottom) phases, respectively. (d) Angle-resolved Raman characterization of the pristine 1T′-$MoTe_2$ (top), lithiated 1T′-$MoTe_2$ (middle) and delithiated 1T′-$MoTe_2$ (bottom) phases, respectively. (e) Diffraction spots and their corresponding intensity profiles of the (002) plane in the reciprocal space by single-crystal XRD collected from the pristine 1T′-$MoTe_2$ at 300 K (top), lithiated 1T′-$MoTe_2$ at 180 K (middle) and delithiated 1T′-$MoTe_2$ at 180 K (bottom) phases, respectively. The dimensions of the nanoflake are 86 μm × 48 μm × ∼100 nm.**

Two-terminal current−voltage measurements were performed to simultaneously monitor the resistance of the 1T′-$MoTe_2$ nanoflake during the phase transitions within the same intercalation cell (Figure 2c). Initially, the resistance of the 1T′-$MoTe_2$ flake remained constant before the phase transition. However, as the V_{EC} ranged between 0.7 and 0.5 V vs Li^+/Li in the lightly lithiated phase I, the resistance increased from 495 Ω at ∼100 min to 577 Ω at ∼237 min. This resistance increase was unexpected, as lithium intercalation in TMDs such as MoS_2 typically results in a decreased resistivity due to the electrons donated by Li.[42] The resistance of the $MoTe_2$ flake further increased to 610 Ω at ∼323 min (V_{EC} = 0.4 V vs Li^+/Li) and increased rapidly exceeding 20 folds compared to 1T′-$MoTe_2$ at V_{EC} = 0.3 V vs Li^+/Li in the heavily lithiated phase II. Since the measurements are two-terminal, the resistance values include contact resistance; however, we confirmed that the observed increased resistivity is not due to the changes in contact resistance (Figure S5). Four-terminal measurements were also performed, as discussed in a later section.

Structural Characterization of the Lithiated 1T′-$MoTe_2$ Flake. We further characterized the structure of the heavily lithiated phase II. We kept V_{EC} = 0.4 V vs Li^+/Li to scrutinize the structural change instead of at V_{EC} = 0.3 V vs Li^+/Li as the latter condition is too close to the amorphization voltage (V_{EC} = 0.2 V vs Li^+/Li). For brevity, we designate the heavily lithiated phase II as lithiated 1T′-$MoTe_2$ in the subsequent discussion. The lithiated 1T′-$MoTe_2$ reverts to the 1T′-$MoTe_2$ upon removal of the V_{EC}. This reversable transformation was studied by *in situ* angle-resolved Raman spectroscopy and *in situ* single-crystal XRD.

https://doi.org/10.1021/acsnano.4c06330
ACS Nano 2024, 18, 17349−17358

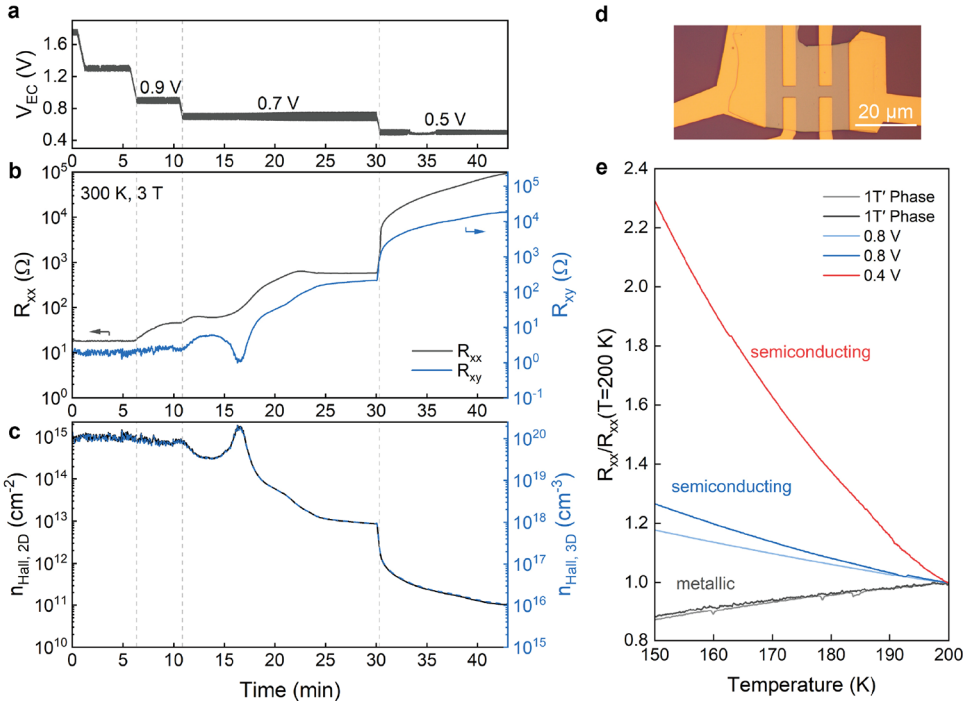

Figure 4. ***In situ*** **Hall measurements of a 1T′-$MoTe_2$ flake (flake dimensions: 28 μm × 26 μm × 97 nm). Profiles of (a) V_{EC}, (b) R_{xx} (black) and R_{xy} (blue), (c) 2D carrier density (left vertical axis, black) and 3D carrier density (right vertical axis, blue) as a function of intercalation time at 3 T and 300 K. (d) Optical image of the 1T′-$MoTe_2$ nanoflake in (a), (b) and (c); scale bar, 20 μm. (e) Zero-field cooling curves of R_{xx} at the pristine 1T′ phase (black), lightly lithiated phase I (blue, V_{EC} = 0.8 V vs Li^+/Li) and heavily lithiated phase II (red, V_{EC} = 0.4 V vs Li^+/Li). Figure S11, S12, and S13 show more characterization of pristine 1T′-$MoTe_2$ and 2H-$MoTe_2$ for comparison.**

In the low frequency region (<50 cm^{-1}) of the Raman spectrum, neither pristine nor delithiated 1T′-$MoTe_2$ show Raman peaks, while lithiated 1T′-$MoTe_2$ displayed a vibration mode at ∼16 cm^{-1} in the parallel polarization as shown in Figure 3b. This peak is distinct from the shear mode of the T_d phase at ∼13 cm^{-1}.[38,43] In the high frequency region (>60 cm^{-1}), several Raman modes appear with unique positions that do not match those observed in the 2H, 1T′ or T_d phases of $MoTe_2$.[38,43] The disappearance of the 1T′-$MoTe_2$ peaks at ∼78 cm^{-1} and ∼127 cm^{-1}, alongside the broadening and shift of the peak at ∼162 cm^{-1}, may be attributed to strain or electron doping introduced by lithium intercalation. However, the increased number of Raman active modes in comparison to the 1T′ phase signifies a transition to a new phase with atomic configurations different from the 1T′ phase. To characterize the crystal symmetry of the new phase, *in situ* angle-resolved Raman spectroscopy was performed, as shown in Figure 3d. Angle-dependent Raman spectra of pristine 1T′-$MoTe_2$, lithiated 1T′-$MoTe_2$ and delithiated 1T′-$MoTe_2$ were collected as a function of the angle between the polarization direction of the incident laser (vertical solid line) and the dashed line shown in Figure 3a. The results showed that the lithium intercalation did not change the 2-fold symmetry of the Raman scattering.

An out-of-plane expansion was observed through the change in the reciprocal lattice of the (002) plane, as determined by *in situ* single-crystal XRD during electrochemical lithiation on individual flakes (Experimental details in Methods). Figure 3e shows the reciprocal lattice of the (002) plane for pristine (top), lithiated phase II (middle) and delithiated (bottom) 1T′-$MoTe_2$. Lithiated 1T′-$MoTe_2$ exhibited two (002) peaks in reciprocal space, indicating a copresence of both pristine 1T′ and lithiated phases. The prominent peak at 2.00 reciprocal lattice units belongs to the pristine 1T′ peak as this peak persisted after delithiation. In contrast to pristine 1T′-$MoTe_2$ which has a peak in reciprocal space at (0,0,2), the peak for lithiated 1T′-$MoTe_2$ is at (0,0,1.87). After converting the data from the reciprocal space to the real space, the *d*-spacing of the (001) plane of lithiated 1T′-$MoTe_2$ was measured to be 7.2850 Å, while that of the pristine and delithiated 1T′-$MoTe_2$ was 6.8115 Å, representing a ∼ 7% expansion in the out-of-plane direction. After the acquisition of single-crystal XRD for the lithiated 1T′-$MoTe_2$, the applied V_{EC} was removed, allowing for the nanoflake to recover to its original 1T′ phase. This recovery was confirmed by the disappearance of the lithiated 1T′-$MoTe_2$ peak. We note that single-crystal XRD was carried out at 180 K to preserve the lithiated phase and to minimize X-ray beam effects (Experimental Methods). At 300 K, the *d*-spacing of the (001) plane of 1T′-$MoTe_2$ was measured to be 6.8115 Å, whereas at 180 K, it was 6.8085 Å, as evidenced by the q vector shift of the (002) plane in reciprocal space (Figure S6). This reduction in the *d*-spacing of the (001) plane was only ∼0.04% and could be attributed either to simple thermal contraction, or the phase transition from the 1T′ to the T_d phase of $MoTe_2$, occurring around ∼250 K.[23,44,45] Figure S7 shows additional single-crystal XRD data of a pristine 1T′-$MoTe_2$ flake taken at 300 K and of a T_d-$MoTe_2$ flake taken at 180 K with further discussions.

In summary, Raman and XRD data indicate that the two new lithiated phases take on different atomic structures from the 1T′ phase. *In situ* transmission electron microscopy (TEM) during lithium intercalation was carried out to show that the in-plane lattice symmetry undergoes a complete transformation in lithiated phase II, in comparison to the initial 1T′ phase, and the lithiated phase II is homogeneous and

https://doi.org/10.1021/acsnano.4c06330
ACS Nano 2024, 18, 17349−17358

single-grained. Figure S8 shows the selected area electron diffraction (SAED) patterns from the $MoTe_2$ flake as Li was inserted using LiO_x as solid electrolyte (Experimental details in Methods, Supplementary Video S1). Despite the clear changes observed in SAED patterns, however, due to experimental complications such as uncontrollable tilting of the flake during intercalation, we could not solve the in-plane lattice structure.

***In Situ* Hall Measurements during Lithium Intercalation.** Compared to the pristine 1T′ phase, the lightly lithiated phase I exhibited a modest increase in the two-terminal electrical resistance, while the heavily lithiated phase II showed over 20-fold increase in resistance. The substantial rise in resistance implies a significant change in the electronic band structure of $MoTe_2$ for the new phases. To probe this, *in situ* Hall measurements were conducted on a 1T′-$MoTe_2$ flake as a function of Li intercalation. Both the longitudinal resistance (R_{xx}) and the Hall resistance (R_{xy}) were measured under a magnetic field strength (B) of 3 T at 300 K, with V_{EC} sweeping from OCV to 0.5 V vs Li^+/Li, as shown in Figure 4a and b. The R_{xx} of the 1T′ phase remained unchanged at 18 Ω during OCV > V_{EC} > 1.1 V vs Li^+/Li. At V_{EC} = 0.7 V vs Li^+/Li, a prompt and substantial rise in R_{xx} was observed, reaching saturation at 579 Ω at ∼30 min, indicating a completion of phase transition from 1T′ to lightly lithiated phase I. Then, the R_{xx} surged to 90 kΩ at ∼42 min at V_{EC} = 0.5 V vs Li^+/Li. The increase of four-point probe R_{xx} agrees with the two-terminal results presented in Figure 2c.

Figure 4c presents the 2D Hall carrier density ($n_{Hall,\ 2D}$) and three-dimensional (3D) Hall carrier density ($n_{Hall,\ 3D}$), derived from the absolute value of R_{xy} using equations outlined in the Experimental Methods section. Within the range of OCV > V_{EC} > 1.1 V vs Li^+/Li, $n_{Hall,\ 2D}$ stayed at 9.7×10^{14} cm^{-2} in the 1T′ phase, with the corresponding $n_{Hall,\ 3D}$ at 1.0×10^{20} cm^{-3} as the thickness of this flake was ∼93.3 nm (Figure S9). At V_{EC} = 0.7 V vs Li^+/Li, $n_{Hall,\ 2D}$ quickly decreased to 8.7×10^{12} cm^{-2} ($n_{Hall,\ 3D}$ at 9.4×10^{17} cm^{-3}) in the lightly lithiated phase I, marking a two-order of magnitude reduction compared to the 1T′ phase. At V_{EC} = 0.5 V vs Li^+/Li at ∼42 min, $n_{Hall,\ 2D}$ further decreased to 1.0×10^{11} cm^{-2} ($n_{Hall,\ 3D}$ at 1.1×10^{16} cm^{-3}).

The reduced carrier density suggests a potential bandgap opening in metallic 1T′-$MoTe_2$ upon lithiation. To substantiate this hypothesis, temperature (T) - dependent R_{xx} curves were obtained for pristine 1T′-$MoTe_2$ (black), lightly lithiated phase I (blue) and heavily lithiated phase II (red), respectively as displayed in Figure 4e. The intercalation cells were rapidly frozen to 200 K to terminate the intercalation and then gradually cooled to 150 K. Resistance values below 150 K were not measured because 150 K represents the glass transition point of the polymer electrolyte where a sudden volume change of the polymer electrolyte breaks the electrical connection of the cell. The resistance of metallic 1T′-$MoTe_2$ decreases with decreasing temperature, as expected. In contrast, lightly lithiated phase I at V_{EC} = 0.8 V vs Li^+/Li and heavily lithiated phase II at V_{EC} = 0.4 V vs Li^+/Li both exhibited semiconductor-like behavior, with their resistance increasing as the temperature decreased. This observation suggests a bandgap opening in the two lithiated phases.

A theoretical paper predicted that a high level of electron doping of over 9×10^{14} e cm^{-2} in monolayer 1T′-$MoTe_2$ introduces lattice distortions and forms a charge density wave (CDW) phase with bandgap opening.[46] We carried out density functional theory (DFT) calculations to test if a bandgap opens in 1T′-$MoTe_2$ upon lithiation. For the atomic structure of the lithiated phase II, we take the measured 7% expansion in the *d*-spacing of the (001) plane and adopt the in-plane lattice structure of the predicted CDW phase, taken from the DFT results of the $MoTe_2$ monolayer study.[46] Using this structure and Li atoms inserted in the vdW gaps, corresponding to a doping level of 9×10^{14} e cm^{-2}, DFT calculations were carried out, which did not show a bandgap opening, even after structural relaxation (Figure S10, Table S3). Thus, we hypothesize that the in-plane lattice structure of the observed lithiated phases may be different from the predicted CDW structure of monolayer $MoTe_2$, which the *in situ* TEM results support (Supplementary Figure S8).

CONCLUSION

In summary, we induced two distinct phases, namely a lightly lithiated phase I and a heavily lithiated phase II, from metallic 1T′-$MoTe_2$ through electrochemical lithium intercalation. The heavily lithiated phase II was characterized by *in situ* angle-resolved Raman spectroscopy, *in situ* single-crystal XRD, and *in situ* TEM. Bandgap opening in the lithiated phases was suggested by *in situ* transport measurements, which showed a significantly reduced Hall carrier density and increasing resistance with decreasing temperature. Successful application of multimodal *in situ* experiments on the electrochemical cells has enabled detailed investigations of the changing structure–property relationship of the TMD nanoflakes during lithium intercalation. This study underscores the efficacy of lithium intercalation as a potent tool for expanding the structural and electronic phase diagram of 2D materials.

EXPERIMENTAL METHODS

Preparation of Coin-Type Cells. 1T′-$MoTe_2$ bulk crystals (HQ Graphene) were ground, sieved (<38 μm), and mixed with 5 weight% acetylene black and 5 weight% polyvinylidene fluoride (PVDF) in n-methyl-2-pyrrolidone (NMP) to form a slurry. The slurry was evenly casted onto a carbon-coated aluminum foil and dried at 50 °C in an argon glovebox overnight, forming the 1T′-$MoTe_2$ cathode sheet with an active loading of approximately 5 mg/cm^2. CR 2032 cells were assembled, utilizing lithium foil as the anode, Celgard 3501 as the separator, battery-grade 1 M lithium hexafluorophosphate ($LiPF_6$ in 50/50 v/v EC/DEC, Sigma-Aldrich) as the electrolyte and either the 1T′-$MoTe_2$ cathode sheet using the ground powder or the 1T′-$MoTe_2$ nanodevice as the cathode.

Device Fabrication. 1T′-$MoTe_2$ nanoflakes were obtained via mechanical exfoliation from 1T′-$MoTe_2$ bulk (HQ Graphene) using scotch-tape onto SiO_2/Si substrates. Following this, a potassium hydroxide (KOH)-assisted transfer method was implemented to select suitable size and thickness of the 1T′-$MoTe_2$ nanoflake.[47] The 1T′-$MoTe_2$ nanoflakes were placed onto dry thermal oxide SiO_2/Si substrates (300 nm SiO_2) with alignment marks designed for subsequent lithography. The thickness of the 1T′-$MoTe_2$ nanoflakes, ranging from 40 to 110 nm, was determined by a Cypher ES atomic force microscope (AFM) from Asylum Research.

Two different methods were used for device fabrication. In the first approach, electrodes were patterned by electron beam lithography (Nabity NPGS, Helios G4 FIB-SEM) and deposited with 10 nm Cr/100 nm Au using electron beam evaporation (PVD Products). Prior to deposition, the sample underwent a 10 min argon etching process. This method was utilized to fabricate devices for *in situ* Raman, *in situ* polarization Raman, and *in situ* Hall transport measurements. The second fabrication approach involved electrodes being written by photolithography (Heidelberg Mask Writer - DWL66FS) and deposited with 10 nm Cr/100 nm Au using an E-gun evaporator (CVC SC4500 Combination Thermal/E-gun Evaporation System). Devices for discharging performance, cyclic voltammetry, and *in situ*

https://doi.org/10.1021/acsnano.4c06330
ACS Nano 2024, 18, 17349−17358

single-crystal XRD measurements were produced with this approach. The fabricated devices were stored in an argon glovebox to minimize oxidation.

Fabrication of Single-Flake Electrochemical Intercalation Cells. All electrochemical intercalation cells were designed with a planar cell configuration, featuring a 1T′-$MoTe_2$ nanoflake as the working electrode and a small piece of lithium metal (∼3 mm by 3 mm, 0.38 mm-thick ribbon, Sigma-Aldrich) as the counter/reference electrode. The detailed process for cell fabrication is described in our previous papers.[34,47,48] The entire cell was encapsulated in a transparent case, with a coverslip serving as the top cover. This design allowed for *in situ* Raman spectroscopy. In the case of liquid intercalation cells, a battery-grade 1 M lithium hexafluorophosphate solution ($LiPF_6$ in 50/50 v/v EC/DEC, Sigma-Aldrich) was injected into the transparent case as the electrolyte. Liquid intercalation cells were only used for discharging performance and cyclic voltammetry measurements. For polymer cells, a blend of 227 mg lithium bis(trifluoromethane)sulfonimide (LiTFSI, Sigma-Aldrich), 475 mg polymer poly(ethylene glycol)methyl ether methacrylate (PEGMA, Sigma-Aldrich) and 1145 mg Bisphenol A ethoxylate (15EO/phenol) dimethacrylate (BEMA, Sigma-Aldrich) was mixed for 4 h. Following this, 46 mg 2-Hydroxy-2-methylpropiophenone (photoinitiator, Sigma-Aldrich) were added to the blend and stirred for an additional half hour in dark prior to use. The blended polymer was carefully injected into the transparent case of the intercalation cell using a micropipette and subsequently cured through exposure to ultraviolet light (UV light, 375 nm, 4 W) for 10 min, forming a solid and stable polymer electrolyte. The assembly of the electrochemical intercalation cells was conducted inside an argon glovebox with O_2 and H_2O levels below 0.5 ppm. The protection provided by the transparent case enabled the intercalation cells to withstand the exposure of air and moisture for a minimum of 10 h, making them suitable for subsequent *in situ* characterizations under atmospheric conditions. For intercalation cells intended for *in situ* Hall transport and *in situ* single-crystal XRD measurements, an ample amount of polymer electrolyte was carefully applied on the device, covering both the 1T′-$MoTe_2$ device and Li, and then cured by UV light for 10 min without the transparent glass case. For those devices without the protection of a transparent case, the cured polymer electrolyte provided sufficient protection for the 1T′-$MoTe_2$ devices and Li against air and moisture. The *in situ* Hall transport and *in situ* single-crystal XRD measurements were conducted under Helium or high-vacuum environment, respectively.

***In Situ* Raman Characterization.** Lithium intercalation of the assembled electrochemical intercalation cell was carried out potentiostatically by applying a voltage between the working (1T′-$MoTe_2$ nanoflake) and counter/reference (Li) electrodes using a Biological SP300 potentiostat/galvanostat. *In situ* Raman spectra were collected during the lithium intercalation using a Horiba LabRAM HR Evolution Spectrometer (grating: 1800 lines/mm) with an excitation wavelength of 633 nm at 10% power (∼3.5 mW).

Prior to intercalation, a Raman spectrum was acquired at the open circuit voltage (OCV), typically ranging between 2.0 to 2.8 V vs Li^+/Li for 1T′-$MoTe_2$ intercalation cells. During electrochemical intercalation, the voltage applied between the 1T′-$MoTe_2$ nanoflake and the lithium electrode (V_{EC}) was lowered at a controlled rate of 10 mV/s, and then maintained at the desired V_{EC} until multiple Raman spectra were collected. Simultaneously, optical images were captured using the camera of a Raman spectroscope. The observed differences in contrast and brightness between the pristine 1T′-$MoTe_2$ and other optical images during the intercalation process were attributed to the presence of the electrolyte and coverslip. Raman mapping was performed using a WITec Alpha300R Confocal Raman Microscope equipped with a grating of 1200 lines/mm, a laser wavelength of 785 nm at 3 mW power to avoid the potential burning effect.

***In Situ* Two-Terminal Electrical Measurements.** *In situ* two-terminal electrical measurements were conducted using a semiconductor device analyzer (Agilent Technologies B1500A) during the lithium intercalation. The drain−source voltage applied was 50 mV, and the resistance was extracted by Ohm's law from the slope of the I−V curve using a linear regression method.

***In Situ* Low-Frequency and Angle-Resolved Raman Characterization.** The low-frequency and angle-resolved Raman spectra were acquired utilizing a Raman spectrometer (HORIBA 550) equipped with a wavelength-stabilized diode laser (785 nm, Topica) at ∼4 mW and 900 lines/mm diffraction grating. The polarization of the incident light was controlled by a half-wave plate and the polarization of the scattered Raman signal was controlled by a linear polarizer. In this work, the collected Raman scattered light was always parallel to the incident light.

***In Situ* Single-Crystal XRD Characterization.** The single-crystal X-ray diffraction (XRD) experiments were carried out at beamline 4-ID Integrated *In situ* and Resonant Hard X-ray Studies (ISR) of National Synchrotron Light Source II at Brookhaven National Laboratory, using a beam energy of 17 keV and spot size of 40 by 300 μm. Prolonged X-ray exposure gradually deteriorated the polymer electrolyte, leading to disconnection of the intercalation cell circuit. A low temperature of 180 K was employed to preserve the lithiated phases even when the intercalation cell is disconnected. The detailed experimental procedure is as follows: a) Initiate the intercalation process on a 1T′-$MoTe_2$ flake at 300 K; b) Lower the temperature from 300 to 180 K at a controlled rate of 10 K/min and conduct X-ray diffraction (XRD) experiments on the lithiated phase; c) Gradually raise the temperature from 180 to 300 K and wait for more than 1 h, during which the lithiated phase reverts back to the delithiated phase; d) Lower the temperature from 300 to 180 K at a rate of 10 K/min and perform XRD experiments on the resulting delithiated phase.

***In Situ* Hall Measurements.** *In situ* Hall measurements were conducted using the quantum design (QD) DynaCool physical property measurement system (PPMS). The 1T′-$MoTe_2$ device was patterned into a Hall bar, assembled to an intercalation cell, positioned and aluminum wire-bonded to PPMS puck, and quickly transferred into the PPMS chamber under full Helium conditions. The device was subjected to electrochemical intercalation at 300 K and a magnetic field strength of 3 T. As a function of intercalation, four-terminal longitudinal voltage drop (V_{xx}) and Hall voltage (V_{xy}) were measured, employing an AC lock-in technique operating at 17.777 Hz with a source current (I_{ds}) of 1 μA and an impedance of 10 MΩ during the intercalation process. The impact of the AC source current of 1 μA from a lock-in amplifier during the intercalation process was evident, causing a potential increase of ∼0.1 V vs Li^+/Li of V_{EC} of phase transition voltage in selected intercalation cells. R_{xx} and R_{xy} were obtained by equations of $R_{xx} = V_{xx}/I_{ds}$ and $R_{xy} = V_{xy}/I_{ds}$. The 2D Hall carrier density ($n_{Hall,\ 2D}$) was calculated by the equation $n_H = B/(e\ R_{xy})$, where the elementary charge $e = 1.602 \times 10^{-19}$ C.[49] The three-dimensional (3D) Hall carrier density ($n_{Hall,\ 3D}$) was calculated by the equation $n_H = B/(e\ t\ R_{xy})$, where t is the thickness of the 1T′-$MoTe_2$ nanoflake measured by AFM. Temperature-dependent resistance measurements were conducted by initially freezing the intercalation cell to 200 K rapidly at a rate of 10 K/min, where the electrochemical intercalation current running through the intercalation cell dropped to nearly zero. Then the system was slowly cooled to 150 K at a rate of 5 K/min.

Postintercalation SEM Characterization. After electrochemical intercalation studies, the cells were dissembled, and the electrolyte was carefully removed. Subsequently, the $MoTe_2$ devices were washed by isopropyl alcohol, dried, and characterized by scanning electron microscopy (HeliosG4 FIB-SEM) at tilt angles of 0° and 40°.

***In Situ* TEM Experiments.** A FEI/ThermoFisher Scientific Titan (60−300 kV) aberration-corrected scanning/transmission electron microscope was used for the *in situ* transmission electron microscopy (TEM) experiments while operating at 300 kV. A specialized probing/biasing Nanofactory Instruments holder was used to simulate a Li/$MoTe_2$ cell within the microscope. The sample was prepared by using silver conductive epoxy to attach small $MoTe_2$ flakes to the end of a copper wire as one electrode and contacting a sharp tungsten wire probe with Li metal within an argon-filled purge box as the other electrode. During the transfer process of the holder from this preparation to within the microscope vacuum, this Li metal on the

https://doi.org/10.1021/acsnano.4c06330
ACS Nano 2024, 18, 17349−17358

tungsten wire was exposed to air resulting in the LiO_x solid electrolyte surface. Once the holder is inserted into the TEM column, the Li-tipped probe can then be positioned to make physical contact with the $MoTe_2$ flakes. At this point a negative potential is applied to the probe to force Li cations through the oxide/hydroxide surface layer of the probe to the intercalate through the $MoTe_2$ flake. During this process the lithiation can be imaged in real or diffraction space as seen in the selected area electron diffraction (SAED) patterns in Figure S8. Some complications however can occur during these types of experiments as the probe contact and then, to a lesser extent, the lithiation process can result in the rotation and straining of the flake. This in turn can lead to inconclusive results regarding the in-plane vs out-of-plane straining of the system when examining the SAED patterns. Additionally, as the reacted area remains on a very small scale relative to the rest of the system, electrochemical cycling information could not be used to identify the voltage and therefore possible phase being imaged at the time. However, this technique was able to demonstrate the overall structural changes of the $MoTe_2$ system.

***Ab Initio* Calculations.** In this study, *ab initio* mean-field calculations for $MoTe_2$ were conducted using density functional theory (DFT) as implemented in the Quantum ESPRESSO package.[50] The calculations utilized optimized norm-conserving Vanderbilt (ONCV) pseudopotentials with the Perdew–Burke–Ernzerhof (PBE) exchange-correlation functional,[51] generated through the ONCVPSP code.[52−54] To ensure DFT convergence, a kinetic cutoff energy of 75 Ry for the plane-wave basis and a convergence threshold of 10^{-8} eV for the change in total energy in each self-consistent step were applied. For the fabricated Li^+ doped bulk phase of $MoTe_2$, the K-points were sampled by a uniform 4 × 4 × 8 grid over the first Brillouin zone. Structural optimizations employed the quasi-Newton method with the maximum ionic Hellmann–Feynman force constrained within 10^{-3} eV. Additionally, spin–orbital coupling (SOC) effects were considered in the calculation of band structures using a relativistic spinor formalism.

XPS Characterization. X-ray photoelectron spectroscopy (XPS) characterization of 1T′-$MoTe_2$ nanoflakes was carried out through Thermo Nexsa G2 XPS Surface Analysis System (Figure S11).

ASSOCIATED CONTENT

Supporting Information

The Supporting Information is available free of charge at https://pubs.acs.org/doi/10.1021/acsnano.4c06330.

Additional galvanostatic discharge and cyclic voltammogram data of $MoTe_2$ powder (Figure S1); post-intercalation SEM images (Figure S2); lithium intercalation of a liquid cell (Figure S3); Raman mapping (Figure S4); repeated cycling of lithiation and delithiation (Figure S5); single-crystal XRD data of 300 and 180 K (Figure S6); single-crystal XRD data of 1T′-$MoTe_2$ and T_d-$MoTe_2$ (Figure S7); *in situ* TEM electron diffraction data (Figure S8); thickness characterization using AFM (Figure S9); DFT calculations (Figure S10); XPS of 1T′-$MoTe_2$ (Figure S11); magneto-transport data of 1T′-$MoTe_2$ (Figure S12); temperature-dependent resistivity of 2H-$MoTe_2$ (Figure S13); Raman comparison tables (Tables S1, S2); atomic positions for DFT calculations (Table S3) (PDF)

Supplementary Video S1 shows the SAED data during the whole lithiation process (MP4)

AUTHOR INFORMATION

Corresponding Author

Judy J. Cha − *Department of Materials Science and Engineering, Cornell University, Ithaca, New York 14853, United States;* orcid.org/0000-0002-6346-2814; Email: jc476@cornell.edu

Authors

Shiyu Xu − *Department of Materials Science and Engineering, Cornell University, Ithaca, New York 14853, United States; Department of Mechanical Engineering and Materials Science, Yale University, New Haven, Connecticut 06511, United States;* orcid.org/0000-0002-3061-632X

Kenneth Evans-Lutterodt − *National Synchrotron Light Source II, Brookhaven National Laboratory, Upton, New York 11973, United States*

Shunran Li − *Department of Chemical and Environmental Engineering, Yale University, New Haven, Connecticut 06511, United States; Energy Sciences Institute, Yale West Campus, West Haven, Connecticut 06516, United States;* orcid.org/0000-0003-0428-295X

Natalie L. Williams − *Department of Materials Science and Engineering, Cornell University, Ithaca, New York 14853, United States; Department of Chemistry and Chemical Biology, Cornell University, Ithaca, New York 14853, United States*

Bowen Hou − *Department of Mechanical Engineering and Materials Science, Yale University, New Haven, Connecticut 06511, United States*

Jason J. Huang − *Department of Materials Science and Engineering, Cornell University, Ithaca, New York 14853, United States;* orcid.org/0000-0002-6387-1650

Matthew G. Boebinger − *Center for Nanophase Materials Sciences, Oak Ridge National Laboratory, Oak Ridge, Tennessee 37830, United States;* orcid.org/0000-0001-9622-2043

Sihun Lee − *Department of Materials Science and Engineering, Cornell University, Ithaca, New York 14853, United States*

Mengjing Wang − *Department of Materials Science and Engineering, Cornell University, Ithaca, New York 14853, United States*

Andrej Singer − *Department of Materials Science and Engineering, Cornell University, Ithaca, New York 14853, United States;* orcid.org/0000-0002-2965-9242

Peijun Guo − *Department of Chemical and Environmental Engineering, Yale University, New Haven, Connecticut 06511, United States; Energy Sciences Institute, Yale West Campus, West Haven, Connecticut 06516, United States;* orcid.org/0000-0001-5732-7061

Diana Y. Qiu − *Department of Mechanical Engineering and Materials Science, Yale University, New Haven, Connecticut 06511, United States;* orcid.org/0000-0003-3067-6987

Complete contact information is available at: https://pubs.acs.org/10.1021/acsnano.4c06330

Author Contributions

S.X. and J.J.C. conceived the project and S.X. carried out the intercalation experiments, Raman characterization, two-terminal electrical measurements, and Hall measurements, with assistance from N.L.W., S.Lee. and M.W. K.E.L. carried out the *in situ* single-crystal XRD characterization. B.H. and D.Y.Q. performed *Ab initio* calculations. S.Li. and P.G. conducted angle-resolved Raman characterization. J.J.H. and A.S. assembled and tested the coin-type cells. M.G.B. carried out the *in situ* TEM characterization. S.X. and J.J.C. wrote the manuscript with input from all authors. All authors have given approval to the final version of the manuscript.

https://doi.org/10.1021/acsnano.4c06330
ACS Nano 2024, 18, 17349−17358

Notes

The authors declare no competing financial interest.

ACKNOWLEDGMENTS

S.X. and J.J.C. gratefully acknowledge support from the National Science Foundation (NSF CBET #2240944). S.L. and P.G. acknowledge the support from the Air Force Office of Scientific Research (Grant No. FA9550-22-1-0209). J.J.H. and A.S. acknowledge the support by the Center for Alkaline-based Energy Solutions, an Energy Frontier Research Center funded by DOE, Office of Science, BES under Award # DE-SC0019445. Device fabrication and characterization were partly carried out at the Yale West Campus Materials Characterization Core and the Yale West Campus Cleanroom. This work was also performed in part at the Cornell NanoScale Facility, a member of the National Nanotechnology Coordinated Infrastructure (NNCI), which is supported by NSF (Grant NNCI-2025233). The authors acknowledge the use of facilities and instrumentation supported by NSF through the Cornell University Materials Research Science and Engineering Center DMR-1719875. This research used beamline 4-ID of the National Synchrotron Light Source II, a U.S. Department of Energy (DOE) Office of Science User Facility operated for the DOE Office of Science by Brookhaven National Laboratory under Contract No. DE-SC0012704. TEM research was conducted as part of a user project at the Center for Nanophase Materials Sciences (CNMS), which is a U.S. DOE, Office of Science User Facility at Oak Ridge National Laboratory. Theory and calculations were supported by the U.S. DOE, Office of Science, Basic Energy Sciences under Early Career Award No. DE-SC0021965. D.Y.Q. acknowledges support by a 2021 Packard Fellowship for Science and Engineering from the David and Lucile Packard Foundation. Development of the BerkeleyGW code was supported by Center for Computational Study of Excited-State Phenomena in Energy Materials (C2SEPEM) at the Lawrence Berkeley National Laboratory, funded by the U.S. DOE, Office of Science, Basic Energy Sciences, Materials Sciences and Engineering Division, under Contract No. DE-C02-05CH11231. The calculations used resources of the National Energy Research Scientific Computing (NERSC), a DOE Office of Science User Facility operated under contract no. DE-AC02-05CH11231; the Advanced Cyberinfrastructure Coordination Ecosystem: Services & Support (ACCESS), which is supported by National Science Foundation grant number ACI-1548562; and the Texas Advanced Computing Center (TACC) at The University of Texas at Austin.

REFERENCES

(1) Iannaccone, G.; Bonaccorso, F.; Colombo, L.; Fiori, G. Quantum Engineering of Transistors Based on 2D Materials Heterostructures. *Nat. Nanotechnol.* **2018**, *13*, 183−191.

(2) Wang, M.; Xu, S.; Cha, J. J. Revisiting Intercalation-Induced Phase Transitions in 2D Group VI Transition Metal Dichalcogenides. *Adv. Energy Sustainability Res.* **2021**, *2*, 2100027.

(3) Mondal, A.; Vomiero, A. 2D Transition Metal Dichalcogenides-Based Electrocatalysts for Hydrogen Evolution Reaction. *Adv. Funct. Mater.* **2022**, *32*, 2208994.

(4) Yang, R.; Fan, J.; Sun, M. Transition Metal Dichalcogenides (TMDCs) Heterostructures: Optoelectric Properties. *Front. Phys.* **2022**, *17*, 43202.

(5) Mia, A. K.; Meyyappan, M.; Giri, P. K. Two-Dimensional Transition Metal Dichalcogenide Based Biosensors: From Fundamentals to Healthcare Applications. *Biosensors (Basel)* **2023**, *13*, 169.

(6) Yang, T.; Wang, Z.; Yuan, J.; Zhou, J.; Yang, M. Emerging Electronic Properties of Polymorphic 2D-TMDs. *In Two-Dimensional Transition-Metal Dichalcogenides* **2024**, 127−179.

(7) Ruppert, C.; Aslan, B.; Heinz, T. F. Optical Properties and Band Gap of Single- and Few-Layer $MoTe_2$ Crystals. *Nano Lett.* **2014**, *14*, 6231−6236.

(8) Hynek, D. J.; Singhania, R. M.; Xu, S.; Davis, B.; Wang, L.; Yarali, M.; Pondick, J. V.; Woods, J. M.; Strandwitz, N. C.; Cha, J. J. cm^2-Scale Synthesis of $MoTe_2$ Thin Films with Large Grains and Layer Control. *ACS Nano* **2021**, *15*, 410−418.

(9) Keum, D. H.; Cho, S.; Kim, J. H.; Choe, D.-H.; Sung, H.-J.; Kan, M.; Kang, H.; Hwang, J.-Y.; Kim, S. W.; Yang, H.; et al. Bandgap Opening in Few-Layered Monoclinic $MoTe_2$. *Nat. Phys.* **2015**, *11*, 482−486.

(10) Song, P.; Hsu, C.-H.; Vignale, G.; Zhao, M.; Liu, J.; Deng, Y.; Fu, W.; Liu, Y.; Zhang, Y.; Lin, H.; et al. Coexistence of Large Conventional and Planar Spin Hall Effect With Long Spin Diffusion Length in a Low-Symmetry Semimetal at Room Temperature. *Nat. Mater.* **2020**, *19*, 292−298.

(11) Sun, Y.; Wu, S.-C.; Ali, M. N.; Felser, C.; Yan, B. Prediction of Weyl Semimetal in Orthorhombic $MoTe_2$. *Phys. Rev. B* **2015**, *92*, 161107.

(12) Qi, Y.; Naumov, P. G.; Ali, M. N.; Rajamathi, C. R.; Schnelle, W.; Barkalov, O.; Hanfland, M.; Wu, S.-C.; Shekhar, C.; Sun, Y.; et al. Superconductivity in Weyl Semimetal Candidate $MoTe_2$. *Nat. Commun.* **2016**, *7*, 11038.

(13) Mandal, M.; Marik, S.; Sajilesh, K. P.; Arushi; Singh, D.; Chakraborty, J.; Ganguli, N.; Singh, R. P. Enhancement of the Superconducting Transition Temperature by Re Doping in Weyl Semimetal $MoTe_2$. *Phys. Rev. Mater.* **2018**, *2*, 094201.

(14) Rhodes, D. A.; Jindal, A.; Yuan, N. F. Q.; Jung, Y.; Antony, A.; Wang, H.; Kim, B.; Chiu, Y.-c.; Taniguchi, T.; Watanabe, K.; et al. Enhanced Superconductivity in Monolayer T_d-$MoTe_2$. *Nano Lett.* **2021**, *21*, 2505−2511.

(15) Dai, X.; Yang, Z.; Li, A.; Yang, J.; Ouyang, F. Character of Defect States in Vacancy-Doped $MoTe_2$ Monolayer: Spatial Localization, Flat Bands and Hybridization Gap. *Superlattices Microstruct.* **2019**, *130*, 528−538.

(16) Wang, Y.; Xiao, J.; Zhu, H.; Li, Y.; Alsaid, Y.; Fong, K. Y.; Zhou, Y.; Wang, S.; Shi, W.; Wang, Y.; et al. Structural Phase Transition in Monolayer $MoTe_2$ Driven by Electrostatic Doping. *Nature* **2017**, *550*, 487−491.

(17) Zakhidov, D.; Rehn, D. A.; Reed, E. J.; Salleo, A. Reversible Electrochemical Phase Change in Monolayer to Bulk-like $MoTe_2$ by Ionic Liquid Gating. *ACS Nano* **2020**, *14*, 2894−2903.

(18) Duerloo, K. A.; Li, Y.; Reed, E. J. Structural Phase Transitions in Two-Dimensional Mo- and W-Dichalcogenide Monolayers. *Nat. Commun.* **2014**, *5*, 4214.

(19) Song, S.; Keum, D. H.; Cho, S.; Perello, D.; Kim, Y.; Lee, Y. H. Room Temperature Semiconductor-Metal Transition of $MoTe_2$ Thin Films Engineered by Strain. *Nano Lett.* **2016**, *16*, 188−193.

(20) Tan, S. J. R.; Abdelwahab, I.; Ding, Z.; Zhao, X.; Yang, T.; Loke, G. Z. J.; Lin, H.; Verzhbitskiy, I.; Poh, S. M.; Xu, H.; et al. Chemical Stabilization of 1T′ Phase Transition Metal Dichalcogenides with Giant Optical Kerr Nonlinearity. *J. Am. Chem. Soc.* **2017**, *139*, 2504−2511.

(21) Eshete, Y. A.; Ling, N.; Kim, S.; Kim, D.; Hwang, G.; Cho, S.; Yang, H. Vertical Heterophase for Electrical, Electrochemical, and Mechanical Manipulations of Layered $MoTe_2$. *Adv. Funct. Mater.* **2019**, *29*, 1904504.

(22) Chen, S.-Y.; Goldstein, T.; Venkataraman, D.; Ramasubramaniam, A.; Yan, J. Activation of New Raman Modes by Inversion Symmetry Breaking in Type II Weyl Semimetal Candidate T′-$MoTe_2$. *Nano Lett.* **2016**, *16*, 5852−5860.

(23) Zhang, K.; Bao, C.; Gu, Q.; Ren, X.; Zhang, H.; Deng, K.; Wu, Y.; Li, Y.; Feng, J.; Zhou, S. Raman Signatures of Inversion Symmetry Breaking and Structural Phase Transition in Ype-II Weyl Semimetal $MoTe_2$. *Nat. Commun.* **2016**, *7*, 13552.

https://doi.org/10.1021/acsnano.4c06330
ACS Nano 2024, 18, 17349−17358

(24) Cho, S.; Kim, S.; Kim, J. H.; Zhao, J.; Seok, J.; Keum, D. H.; Baik, J.; Choe, D.-H.; Chang, K. J.; Suenaga, K.; et al. Phase Patterning for Ohmic Homojunction Contact in $MoTe_2$. *Science* **2015**, *349*, 625−628.
(25) Datye, I. M.; Rojo, M. M.; Yalon, E.; Deshmukh, S.; Mleczko, M. J.; Pop, E. Localized Heating and Switching in $MoTe_2$-Based Resistive Memory Devices. *Nano Lett.* **2020**, *20*, 1461−1467.
(26) Hou, W.; Azizimanesh, A.; Sewaket, A.; Peña, T.; Watson, C.; Liu, M.; Askari, H.; Wu, S. M. Strain-Based Room-Temperature Non-Volatile $MoTe_2$ Ferroelectric Phase Change Transistor. *Nat. Nanotechnol.* **2019**, *14*, 668−673.
(27) He, Y.; Boubeche, M.; Zhou, Y.; Yan, D.; Zeng, L.; Wang, X.; Yan, K.; Luo, H. Topologically Nontrivial 1T'-$MoTe_2$ as Highly Efficient Hydrogen Evolution Electrocatalyst. *J. Phys.: Mater.* **2021**, *4*, 014001.
(28) Panda, M. R.; Gangwar, R.; Muthuraj, D.; Sau, S.; Pandey, D.; Banerjee, A.; Chakrabarti, A.; Sagdeo, A.; Weyland, M.; Majumder, M.; et al. High Performance Lithium-Ion Batteries Using Layered 2H-$MoTe_2$ as Anode. *Small* **2020**, *16*, 2002669.
(29) Xiong, F.; Wang, H.; Liu, X.; Sun, J.; Brongersma, M.; Pop, E.; Cui, Y. Li Intercalation in MoS_2: In Situ Observation of Its Dynamics and Tuning Optical and Electrical Properties. *Nano Lett.* **2015**, *15*, 6777−6784.
(30) Rajapakse, M.; Karki, B.; Abu, U. O.; Pishgar, S.; Musa, M. R. K.; Riyadh, S. M. S.; Yu, M.; Sumanasekera, G.; Jasinski, J. B. Intercalation as a Versatile Tool for Fabrication, Property Tuning, and Phase Transitions in 2D Materials. *npj 2D Mater. Appl.* **2021**, *5*, 30.
(31) Ambrosi, A.; Sofer, Z.; Pumera, M. 2H → 1T Phase Transition and Hydrogen Evolution Activity of MoS_2, $MoSe_2$, WS_2 and WSe_2 Strongly Depends on the MX_2 Composition. *Chem. Commun.* **2015**, *51*, 8450−8453.
(32) Tian, L.; Qiao, H.; Huang, Z.; Qi, X. Li-Ion Intercalated Exfoliated WS_2 Nanosheets with Enhanced Electrocatalytic Hydrogen Evolution Performance. *Cryst. Res. Technol.* **2021**, *56*, 2000165.
(33) Muscher, P. K.; Rehn, D. A.; Sood, A.; Lim, K.; Luo, D.; Shen, X.; Zajac, M.; Lu, F.; Mehta, A.; Li, Y.; et al. Highly Efficient Uniaxial In-Plane Stretching of a 2D Material via Ion Insertion. *Adv. Mater.* **2021**, *33*, 2101875.
(34) Wang, M.; Kumar, A.; Dong, H.; Woods, J. M.; Pondick, J. V.; Xu, S.; Hynek, D. J.; Guo, P.; Qiu, D. Y.; Cha, J. J. A Gapped Phase in Semimetallic T_d-WTe_2 Induced by Lithium Intercalation. *Adv. Mater.* **2022**, *34*, 2200861.
(35) Xu, S.; Wang, M.; Bambrick-Santoyo, M.; Evans-Lutterodt, K.; Williams, N. L.; Cha, J. J. Role of Heterointerface in Lithium-Induced Phase Transition in T_d-WTe_2 Nanoflakes. *ACS Appl. Elect. Mater.* **2024**, *6*, 785−792.
(36) Selwyn, L. S.; McKinnon, W. R.; von Sacken, U.; Jones, C. A. Lithium Electrochemical Cells at Low Voltage: Decomposition of Mo and W Dichalcogenides. *Solid State Ionics* **1987**, *22*, 337−344.
(37) Zhang, J.; Yang, A.; Wu, X.; van de Groep, J.; Tang, P.; Li, S.; Liu, B.; Shi, F.; Wan, J.; Li, Q.; et al. Reversible and Selective Ion Intercalation Through the Top Surface of Few-Layer MoS_2. *Nat. Commun.* **2018**, *9*, 5289.
(38) Cheon, Y.; Lim, S. Y.; Kim, K.; Cheong, H. Structural Phase Transition and Interlayer Coupling in Few-Layer 1T′ and T_d $MoTe_2$. *ACS Nano* **2021**, *15*, 2962−2970.
(39) Hart, J. L.; Bhatt, L.; Zhu, Y.; Han, M.-G.; Bianco, E.; Li, S.; Hynek, D. J.; Schneeloch, J. A.; Tao, Y.; Louca, D.; et al. Emergent Layer Stacking Arrangements in C-axis Confined $MoTe_2$. *Nat. Commun.* **2023**, *14*, 4803.
(40) Kufian, M. Z.; Majid, S. R. Performance of Lithium-Ion Cells Using 1 M LiPF6 in EC/DEC (v/v = 1/2) Electrolyte With Ethyl Propionate Additive. *Ionics* **2010**, *16*, 409−416.
(41) Nair, J. R.; Gerbaldi, C.; Destro, M.; Bongiovanni, R.; Penazzi, N. Methacrylic-Based Solid Polymer Electrolyte Membranes for Lithium-Based Batteries by a Rapid UV-Curing Process. *React. Funct. Polym.* **2011**, *71*, 409−416.
(42) Eda, G.; Yamaguchi, H.; Voiry, D.; Fujita, T.; Chen, M.; Chhowalla, M. Photoluminescence from Chemically Exfoliated MoS_2. *Nano Lett.* **2011**, *11*, 5111−5116.
(43) Ma, X.; Guo, P.; Yi, C.; Yu, Q.; Zhang, A.; Ji, J.; Tian, Y.; Jin, F.; Wang, Y.; Liu, K.; et al. Raman Scattering in the Transition-Metal Dichalcogenides of 1T'-$MoTe_2$, T_d-$MoTe_2$, and T_d-WTe_2. *Phys. Rev. B* **2016**, *94*, 214105.
(44) Clarke, R.; Marseglia, E.; Hughes, H. P. A Low-Temperature Structural Phase Transition in β-$MoTe_2$. *Philos. Mag. B* **1978**, *38*, 121−126.
(45) Itahashi, Y. M.; Nohara, Y.; Ideue, T.; Akiba, T.; Takahashi, H.; Ishiwata, S.; Iwasa, Y. Low-Temperature Phase Transition in Polar Semimetal T_d-$MoTe_2$ Probed by Nonreciprocal Transport. *Phys. Rev. Res.* **2023**, *5*, L022022.
(46) Lee, J.-H.; Son, Y.-W. Gate-Tunable Superconductivity and Charge-Density Wave in Monolayer 1T'-$MoTe_2$ and 1T'-WTe_2. *Phys. Chem. Chem. Phys.* **2021**, *23*, 17279−17286.
(47) Yazdani, S.; Pondick, J. V.; Kumar, A.; Yarali, M.; Woods, J. M.; Hynek, D. J.; Qiu, D. Y.; Cha, J. J. Heterointerface Effects on Lithium-Induced Phase Transitions in Intercalated MoS_2. *ACS Appl. Mater. & Inter.* **2021**, *13*, 10603−10611.
(48) Pondick, J. V.; Kumar, A.; Wang, M.; Yazdani, S.; Woods, J. M.; Qiu, D. Y.; Cha, J. J. Heterointerface Control over Lithium-Induced Phase Transitions in MoS_2 Nanosheets: Implications for Nanoscaled Energy Materials. *ACS Appl. Nano Mater.* **2021**, *4*, 14105−14114.
(49) Bediako, D. K.; Rezaee, M.; Yoo, H.; Larson, D. T.; Zhao, S. Y. F.; Taniguchi, T.; Watanabe, K.; Brower-Thomas, T. L.; Kaxiras, E.; Kim, P. Heterointerface Effects in the Electrointercalation of Van Der Waals heterostructures. *Nature* **2018**, *558*, 425−429.
(50) Giannozzi, P.; Baroni, S.; Bonini, N.; Calandra, M.; Car, R.; Cavazzoni, C.; Ceresoli, D.; Chiarotti, G. L.; Cococcioni, M.; Dabo, I.; et al. QUANTUM ESPRESSO: a Modular and Open-Source Software Project for Quantum Simulations of Materials. *J. Phys.: Condens.Matter* **2009**, *21*, 395502.
(51) Perdew, J. P.; Burke, K.; Ernzerhof, M. Generalized Gradient Approximation Made Simple. *Phys. Rev. Lett.* **1996**, *77*, 3865−3868.
(52) Hamann, D. R. Optimized Norm-Conserving Vanderbilt Pseudopotentials. *Phys. Rev. B* **2013**, *88*, 085117.
(53) Schlipf, M.; Gygi, F. Optimization Algorithm for the Generation of ONCV Pseudopotentials. *Comput. Phys. Commun.* **2015**, *196*, 36−44.
(54) Scherpelz, P.; Govoni, M.; Hamada, I.; Galli, G. Implementation and Validation of Fully Relativistic GW Calculations: Spin-Orbit Coupling in Molecules, Nanocrystals, and Solids. *J. Chem. Theory Comput.* **2016**, *12*, 3523−3544.

https://doi.org/10.1021/acsnano.4c06330
ACS Nano 2024, 18, 17349−17358